


Cite this: *RSC Adv.*, 2021, **11**, 28466

$B_{12}X_{11}(H_2)^-$: exploring the limits of isotopologue selectivity of hydrogen adsorption[†]

Toshiki Wulf, ^{*ab} Jonas Warneke ^{ac} and Thomas Heine ^{*bd}

We study the isotopologue-selective binding of dihydrogen at the undercoordinated boron site of $B_{12}X_{11}^-$ ($X = H, F, Cl, Br, I, CN$) using *ab initio* quantum chemistry. With a Gibbs free energy of H_2 attachment reaching up to 80 kJ mol^{-1} (ΔG at 300 K for $X = CN$), these sites are even more attractive than most undercoordinated metal centers studied so far. We thus believe that they can serve as an edge case close to the upper limit of isotopologue-selective H_2 adsorption sites. Differences of the zero-point energy of attachment average 5.0 kJ mol^{-1} between D_2 and H_2 and 2.7 kJ mol^{-1} between HD and H_2 , resulting in hypothetical isotopologue selectivities as high as 2.0 and 1.5, respectively, even at 300 K . Interestingly, even though attachment energies vary substantially according to the chemical nature of X , isotopologue selectivities remain very similar. We find that the H – H activation is so strong that it likely results in the instantaneous heterolytic dissociation of H_2 in all cases (except, possibly, for $X = H$), highlighting the extremely electrophilic nature of $B_{12}X_{11}^-$ despite its negative charge. Unfortunately, this high reactivity also makes $B_{12}X_{11}^-$ unsuitable for practical application in the field of dihydrogen isotopologue separation. Thus, this example stresses the two-edged nature of strong H_2 affinity, yielding a higher isotopologue selectivity on the one hand but risking dissociation on the other, and helps define a window of adsorption energies into which a material for selective adsorption near room temperature should ideally fall.

Received 20th August 2021
Accepted 1st September 2021

DOI: 10.1039/d1ra06322g
rsc.li/rsc-advances

Introduction

As the element with the lowest mass, hydrogen has the most pronounced isotope effect of all elements. This leads to numerous applications of heavy hydrogen isotopes, deuterium ($^2\text{H} = D$) and tritium ($^3\text{H} = T$): in spectroscopy; structural analysis and the elucidation of reaction mechanisms, especially in biochemistry and pharmaceutical research;^{1,2} and – more recently – even in pharmaceuticals,^{3,4} where an effort is ongoing to exploit the slower rate of reaction of deuterated compounds to delay or alter metabolic pathways in order to increase potency and/or reduce side effects.

The continuous need for heavy hydrogen for energy production, science and medicine has motivated a revision of state-of-the-art

separation processes⁵ by employing nanostructured materials. In a relatively recent approach, penetration and tunneling through two-dimensional materials such as graphene or hexagonal boron nitride are used to separate hydrogen isotopes.^{6,7} Other separation techniques involve kinetic sieving in the interstitial space of layered materials⁸ or in apertures in metal–organic frameworks (MOFs),⁹ or isotopologue-selective adsorption (chemical affinity quantum sieving, CAQS)¹⁰ at strong metal sites in MOFs^{11–13} and zeolites.^{14,15}

CAQS relies on the different zero-point energies of the H_2 isotopologues, which approximately correlate with the square root of the mass of the isotopologue. This leads to a stronger adsorption of the heavier isotopes and results in higher selectivities when the zero-point energy of adsorption is higher. The adsorption energy itself also positively correlates with the selectivity (albeit more loosely), because a higher adsorption energy leads to a steeper potential energy surface, which in turn increases the zero-point energy. (Although the stretching of the H – H bond decreases the frequency of the corresponding vibrational mode and thereby the zero-point energy, this effect is overcompensated by the contributions from other modes.^{16,17})

Recent progress has been made to enable CAQS significantly above the boiling temperature of liquid nitrogen. For example, Cu(I)-MFU-4l with an H_2 adsorption enthalpy on the order of $30\text{--}35 \text{ kJ mol}^{-1}$ and a zero-point energy difference of $2.5\text{--}3.0 \text{ kJ mol}^{-1}$ between D_2 and H_2 reaches a D_2/H_2 selectivity of 10 at 100 K . However, since both selectivity and uptake decline with

^aWilhelm Ostwald Institute of Physical and Theoretical Chemistry, Leipzig University, Linnéstr. 2, 04103 Leipzig, Germany. E-mail: toshiki.wulf@uni-leipzig.de

^bInstitute of Resource Ecology, Research Site Leipzig, Helmholtz-Zentrum Dresden-Rossendorf, Permoserstr. 15, 04318 Leipzig, Germany. E-mail: thomas.heine@tu-dresden.de

^cLeibniz Institute of Surface Engineering (IOM), Permoserstr. 15, 04318 Leipzig, Germany

^dFaculty of Chemistry and Food Chemistry, School of Science, TU Dresden, 01062 Dresden, Germany

[†] Electronic supplementary information (ESI) available: Additional tables and figures as quoted in the article (PDF); sample input files (TXT); atomic coordinates and NEB paths (XYZ); and vibration files (7-column XYZ, which can be read and visualized *e.g.* with Jmol²⁰ using tools → vibrate). See DOI: 10.1039/d1ra06322g



increasing temperature, operating temperatures must remain well below 200 K.¹² Nevertheless, these experiments raised hopes that an appreciable selectivity at or near room temperature could be achieved if materials or adsorption sites with higher adsorption energies could be found. With this publication, we want to make a contribution towards the search of such materials.

$B_{12}X_{11}^-$ is a fascinating ion. Derived from the highly stable^{18–20} dianion $B_{12}X_{12}^{2-}$ by abstraction of X^- , its reactivity is driven by the strong preference for a double negative charge.^{21,22} Despite its negative charge, the monoanion is therefore highly electron-deficient. The partial positive charge at the under-coordinated boron atom would be expected to lead to strong H_2 attraction in a way similar to undercoordinated metal cations.¹⁷ The significant interaction between the undercoordinated boron site and noble gas atoms reported by experiment and theory^{21–24} suggests that this system will also strongly bind dihydrogen, and that gas-phase experiments addressing this interaction should be feasible. A particularly attractive feature of these systems is the prospect of modifying the substituents X in order to form a cavity that sterically confines the bound dihydrogen to further increase isotopologue selectivity. For these reasons, we consider $B_{12}X_{11}^-$ a suitable model system to study the limits of isotopologue-selective H_2 adsorption.

In this article, we computationally study H_2 attachment at $B_{12}X_{11}^-$ (X = H, F, Cl, Br, I, CN). Using *ab initio* methods, we calculate thermodynamic parameters of the attachment reaction, analyze the influence of X on these parameters and of the different vibrational modes on the isotopologue selectivity. Furthermore, we investigate entropy effects, calculate isotopologue selectivities of the hypothetical adsorption of molecular H_2 and examine potential dissociation pathways for H_2 bound at $B_{12}X_{11}^-$. Therefore, the present study highlights a wide range of aspects that are useful for the rational design of materials for dihydrogen isotopologue separation, including some rather surprising findings on the relation of attachment energy and selectivity, parameters that can be adjusted to enhance selectivity, and obstacles such as dihydrogen dissociation.

Methods

$B_{12}X_{11}^-$ (with X = H, F, Cl, Br, I and CN) and their H_2 adducts have been optimized with hybrid density functional theory using the PBE0 (ref. 25) functional. Dispersion interactions have been accounted for with Grimme's D3 approach and Becke-Johnson damping, commonly referred to as D3(BJ).²⁶ Equilibrium structures, their energies and Hirshfeld charges have been obtained using geometry optimization employing Ahlrich's def2-QZVP split-valence quadruple-zeta basis set.²⁷ Potential energy surface scans have been performed using the smaller def2-TZVP basis set from the same series. For all DFT calculations we have made use of the resolution-of-identity and chain-of-spheres approximations, RIJ-COSX,²⁸ in conjunction with the def2/J²⁹ auxiliary basis.

Thermal and zero-point energy contributions to enthalpies and entropies have been calculated at the above-mentioned DFT level using numerical harmonic vibrational frequency analysis. Standard increments of 0.005 Bohr have been used except for $B_{12}H_{11}(H_2)^-$ and $B_{12}F_{11}(H_2)^-$ where this led to

imaginary frequencies; 0.002 and 0.001 Bohr, respectively, have been used in those cases to ensure consistent treatment in thermodynamic calculations by ORCA. The Gibbs free energy has been calculated using the quasi-rigid-rotor-harmonic-oscillator (QRRHO) approximation³⁰ as implemented in ORCA. This approximation treats the entropy (but not internal energy) contributions of low-frequency vibrational modes as free internal rotations by default. In line with such treatment, the zero-point and thermal vibrational contributions of the internal rotation to the internal energy have been subtracted from the value calculated by ORCA and $\frac{1}{2}RT$ has been added instead. Finally, entropy contributions have been corrected for an external symmetry number of 5 for $B_{12}X_{11}^-$ and an internal symmetry number for $B_{12}X_{11}(H_2)^-$: 10 for homoisotopic cases and 5 for heteroisotopic ones.³¹ For the $B_{12}X_{11}(H_2)^-$ species, the Gibbs energies have been calculated for both symmetrical orientations of H_2 with respect to $B_{12}X_{11}^-$ and the average has been used subsequently.

The hypothetical separation factors between two isotopologues of H_2 (below referred to as *i* and *j*) have been calculated from the Gibbs energies of attachment of H_2 (for the reaction leading to the local minima with undissociated H_2) *via* the respective equilibrium constants:

$$S_{ij} = \frac{K_i}{K_j} = \exp\left(\frac{-\Delta\Delta G}{R T}\right) \text{ where } \Delta\Delta G = \Delta G_i - \Delta G_j$$

Correlated single-point calculations have been performed using the DLPNO-CCSD(T)^{32,33} method as implemented in ORCA in conjunction with the def2-QZVPP and def2-QZVPP/C³⁴ basis sets based on a Hartree-Fock calculation with VeryTightSCF settings. SCF convergence issues, which arose in some cases, have been cured using the SlowConv setting and employing the SOSCF algorithm late in the SCF procedure (SOSCFStart 0.0001). For X = H, NormalPNO and TightPNO³⁵ settings have been compared and found to give almost identical results; NormalPNO has therefore been used throughout. Similarly, def2-TZVPP, def2-QZVPP, aug-cc-pVTZ and aug-cc-pVQZ basis sets have been found to yield very similar reaction energies for X = H, which has been taken as justification for using def2-QZVPP results without further refinement or correction for basis set effects.

Calculations employed ORCA³⁶ version 4.2.1, except for energy decomposition analysis (EDA). The latter calculations have been performed with the Amsterdam Density Functional (ADF) program from the Amsterdam Modeling Suite (AMS), version 2019.104 (r76620),^{37,38} performing single-point calculations at the PBE0-D3(BJ) level in conjunction with scalar ZORA³⁹ for relativistic effects and the TZ2P⁴⁰ basis set with native Slater-type orbitals.

Results and discussion

Structure of $B_{12}X_{11}^-$ and $B_{12}X_{11}(H_2)^-$

The structure of $B_{12}X_{11}^-$ (X = F, Cl, Br, I, CN) with and without attached noble gas atoms has been computationally investigated several times^{21–23} and discussed in detail recently.²⁴ Compared to $B_{12}X_{12}^{2-}$, the undercoordinated boron atom (B^0) in $B_{12}X_{11}^-$ moves toward the center of the cluster. Meanwhile, the substituents X of



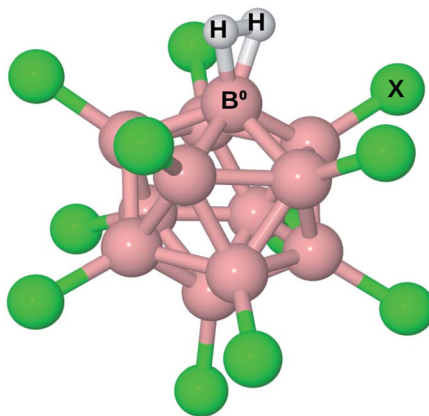


Fig. 1 Illustration of $\text{B}_{12}\text{X}_{11}^-$ with H_2 attached. B^0 is the boron atom which is undercoordinated in $\text{B}_{12}\text{X}_{11}^-$ and to which H_2 is bound in $\text{B}_{12}\text{X}_{11}(\text{H}_2)^-$.

Table 1 Characteristic geometric parameters of $\text{B}_{12}\text{X}_{11}(\text{H}_2)^-$: H–H bond length (minimum on the potential energy surface at the PBE0-D3(BJ) level) and distance between B^0 and center of H_2 . All distances in pm

X	$r(\text{H}-\text{H})$	$R(\text{B}^0-\text{H}_2)$
(Free H_2)	74.4	
H	85.0	125.7
F	91.0	119.6
Cl	85.2	125.2
Br	84.5	126.4
I	84.1	127.6
CN	84.2	127.3

the surrounding boron atoms slightly bend towards B^0 , thereby decreasing the angle $\alpha(\text{X}-\text{Ctr}-\text{B}^0)$ between X, the center of the cluster (Ctr) and B^0 from 63.4° to 60.5° . Upon binding of noble gas atoms, this angle remains practically unchanged.

Given the similar size of He, Ne and H_2 , one might expect $\text{B}_{12}\text{X}_{11}(\text{H}_2)^-$ to behave similarly to $\text{B}_{12}\text{X}_{11}\text{He}^-$ and $\text{B}_{12}\text{X}_{11}\text{Ne}^-$. However, the latter two complexes show distinct differences in their B^0 –noble gas bond length. Moreover, H_2 has a much higher HOMO, lower LUMO and is more polarizable. Therefore, it should bind much more strongly to $\text{B}_{12}\text{X}_{11}^-$. This expectation

is reflected in the B^0 – H_2 distances, which are much shorter than those of B^0 –He despite similar sizes.

The structure of $\text{B}_{12}\text{X}_{11}(\text{H}_2)^-$ is shown in Fig. 1. For all X investigated, the H–H bond is elongated by more than 9 pm, that is at least 3 pm more than for H_2 coordinated at $(\text{C}_4\text{H}_8\text{O}_2)\text{Cu}^+$ ($\text{C}_4\text{H}_8\text{O}_2$ = 1,4-dioxane; calculated value from ref. 17). A comparison of the geometric parameters, which are listed in Table 1, reveals that $\text{X} = \text{F}$ is an outlier with a much longer H–H bond length and a shorter B^0 – H_2 distance, which has consequences for the thermodynamic properties and isotopologue selectivity as discussed below.

Analysis of the dihydrogen– $\text{B}_{12}\text{X}_{11}^-$ interaction

Attachment energies for H_2 coordinating side-on at $\text{B}_{12}\text{X}_{11}^-$ are shown in Table 2 and have, with the exception of $\text{X} = \text{H}$, a magnitude of $\approx 100 \text{ kJ mol}^{-1}$, which is much stronger than for most interactions of H_2 with undercoordinated metal sites.^{11,12} As would be expected from the significantly elongated H–H bonds, the title compounds are predicted to strongly attract H_2 . However, the order $\text{CN} \approx \text{F} > \text{Cl} \gtrsim \text{Br} > \text{I} \gg \text{H}$ from strongest to weakest interaction differs from what would be expected from the bond lengths (Table 1). This surprising lack of correlation, which is shown in Fig. 2a, is contrary to systems where undercoordinated metal sites serve as attractors and where bond length and binding energy are evidently correlated.

Interestingly, the H–H bond is much more elongated for $\text{X} = \text{F}$ compared to other X, despite a binding energy which is only slightly higher. Conversely, $\text{X} = \text{H}$ shows a substantially lower binding energy (36 kJ mol^{-1} vs. $> 90 \text{ kJ mol}^{-1}$) despite geometric parameters which are very similar to $\text{X} = \text{Cl}$. Furthermore, $\text{X} = \text{CN}$, which has the second-highest H_2 binding energy after $\text{X} = \text{F}$, lies in between the least strongly binding halogens $\text{X} = \text{Br}$ and $\text{X} = \text{I}$ in terms of the H–H bond length. Only for $\text{X} = \text{Cl}$, Br , I does the binding energy follow the trend expected from the DFT-predicted bond lengths, that is: among the three, $\text{B}_{12}\text{Cl}_{11}(\text{H}_2)^-$ has the highest binding energy, the shortest B^0 – H_2 distance and the most elongated H–H bond, followed by $\text{B}_{12}\text{Br}_{11}(\text{H}_2)^-$ with $\text{B}_{12}\text{I}_{11}(\text{H}_2)^-$ being last.

If the interaction between H_2 and all investigated $\text{B}_{12}\text{X}_{11}^-$ was mainly driven by σ bonding (from H_2 to B^0), one would expect a strong correlation between the charge at B^0 and the H_2 attachment energy. At least for Cl, Br and I, a reasonable

Table 2 Internal energies of H_2 and D_2 attachment at $\text{B}_{12}\text{X}_{11}^-$ calculated for 0 K, difference of this energy between D_2 and H_2 (which is equivalent to the difference in zero-point energy), Gibbs energies of attachment for 300 K, its difference between D_2 and H_2 and the resulting D_2/H_2 selectivity at 300 K. All energies are in kJ mol^{-1} ; selectivities in units of one

X =	$\Delta_{\text{ad}}U(\text{H}_2)$	$\Delta_{\text{ad}}U(\text{D}_2)$	$\Delta\Delta E_0$	$\Delta_{\text{ad}}G(\text{H}_2)$	$\Delta_{\text{ad}}G(\text{D}_2)$	$\Delta\Delta G$	$S(\text{D}_2/\text{H}_2)$
H	-36.6	-41.5	-4.9	-9.1	-10.8	-1.72	1.99
F	-110.0	-114.6	-4.6	-81.3	-82.6	-1.31	1.69
Cl	-101.4	-106.6	-5.2	-72.5	-74.3	-1.81	2.06
Br	-98.5	-103.6	-5.2	-70.1	-71.9	-1.77	2.04
I	-90.4	-95.4	-5.1	-62.0	-63.7	-1.67	1.96
CN	-108.5	-113.9	-5.3	-80.0	-81.8	-1.87	2.12



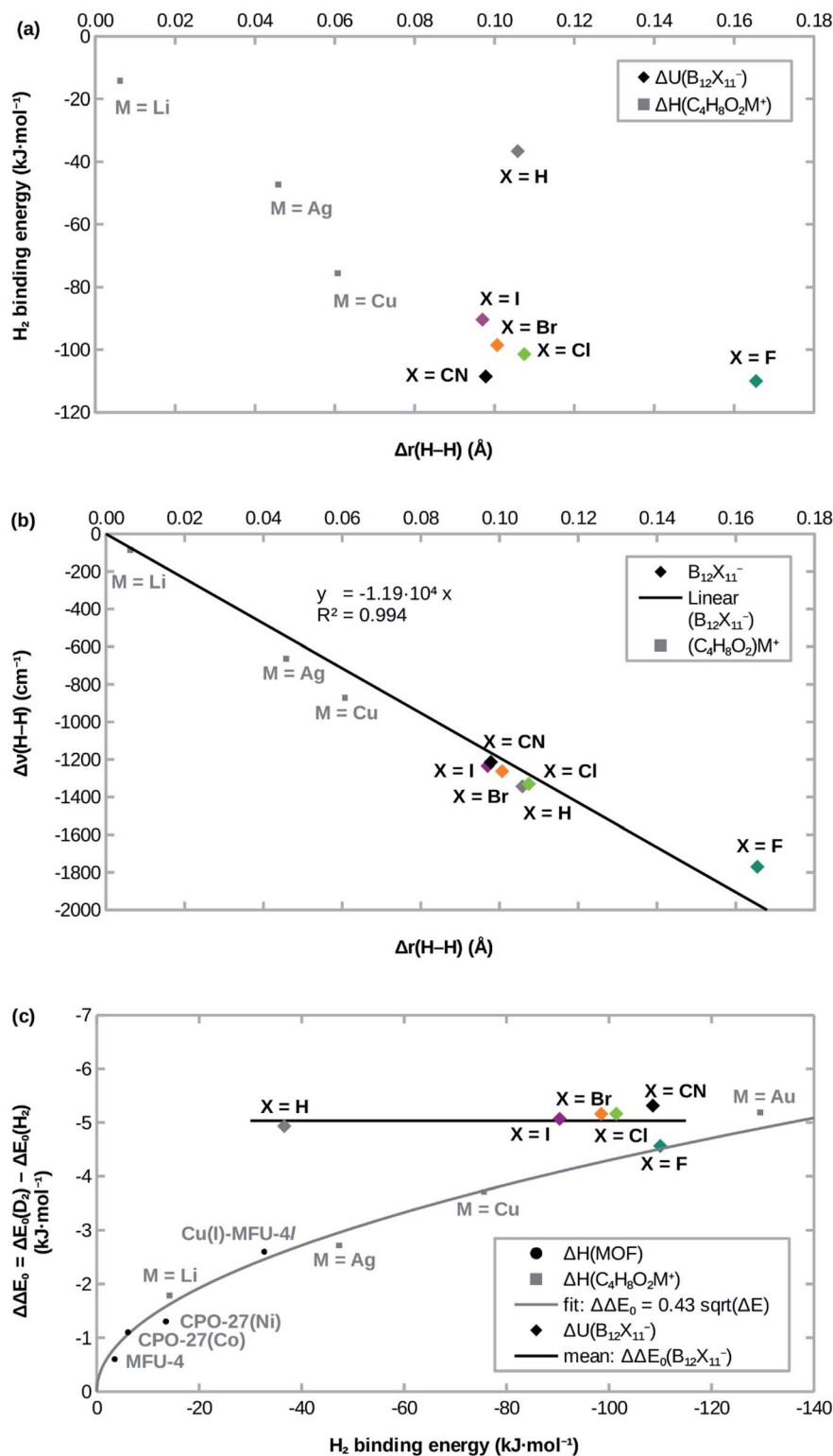


Fig. 2 Correlation of (a) the H₂ attachment energy and (b) the red-shift of H–H stretch frequency $\Delta\nu(H–H)$ with the H–H bond length elongation $\Delta r(H–H)$ w.r.t. free H₂ in $B_{12}X_{11}^-$ and dioxane complexes. (c): Comparison of H₂ attachment energies and differences of zero-point energies of attachment $\Delta\Delta E_0$ between D₂ and H₂. Experimental values for MOFs are from ref. 12,13,41, calculated values for dioxane complexes ($C_4H_8O_2M^+$) are from ref. 17.

correlation between attachment energy and Hirshfeld charge at B⁰ is found (see ESI; Fig. S1†). However, the correlation is poor for other X and different charge trends are obtained when using

orbital-based charges such as NPA charges (Fig. S2†). Furthermore, this does not explain the significant elongation of the H–H bond for X = F.

Table 3 Contributions to the Gibbs free energy of attachment (300 K) of H_2 at $\text{B}_{12}\text{X}_{11}^-$ from energy decomposition analysis (EDA): Pauli repulsion energy ΔE_{Pauli} , electrostatic interaction (including nuclear repulsion) ΔE_{elstat} , orbital interaction ΔE_{oi} , explicit dispersion correction ΔE_{disp} , geometry deformation ΔE_{def} of $\text{B}_{12}\text{X}_{11}^-$ and H_2 , Born–Oppenheimer energy ΔE_{el} (sum of electronic and nuclear contributions, *i.e.* all of the aforementioned ones), zero-point energy ΔE_0 , thermal contributions ΔE_{therm} at 300 K (mostly entropy) and total Gibbs energy ΔG (sum of ΔE_{el} , ΔE_0 and ΔE_{therm}). ΔG values differ from Table 2 because EDA is at the DFT level; values in Table 2 are expected to be more accurate. All energies in kJ mol^{-1}

X =	ΔE_{Pauli}	ΔE_{elstat}	ΔE_{oi}	ΔE_{disp}	$\Delta E_{\text{def}}(\text{B}_{12}\text{X}_{11}^-)$	$\Delta E_{\text{def}}(\text{H}_2)$	ΔE_{el}	ΔE_0	ΔE_{therm}	ΔG
CN	400	−166	−402	−10	13	19	−146	22	29	−95
Cl	435	−185	−405	−10	16	16	−134	22	29	−84
Br	444	−185	−406	−11	14	14	−130	21	28	−81
I	476	−192	−420	−13	13	13	−122	21	28	−73
H	490	−205	−385	−7	15	19	−72	21	27	−23
F	480	−213	−462	−7	34	18	−150	23	29	−99

Since these unintuitive findings warrant a deeper investigation of the underlying binding properties, we have performed energy decomposition analysis (EDA) of the Gibbs energy of the attachment reaction of H_2 at $\text{B}_{12}\text{X}_{11}^-$. Results are shown in Table 3: With one exception (ΔE_{def} of $\text{B}_{12}\text{X}_{11}^-$, for discussion see below), the contributions of dispersion interaction and geometry deformation of the reactants as well as zero-point and thermal contributions are very similar.

The greatest variability is afforded by the Pauli repulsion term, which results from the antisymmetry requirement of the wave function and closely matches the intuitive understanding of steric repulsion. For CN, Cl, Br and I, Pauli repulsion is the dominating contributor to the overall trend in the reaction Gibbs energies. It is partly compensated by the electrostatic interaction, which may sound surprising at first, but is justified given the well-known fact⁴² that molecules attract each other more strongly the more diffuse their charge clouds are.

EDA shows two main reasons for the $\text{B}_{12}\text{X}_{11}^-$ – H_2 interaction being weakest for $\text{X} = \text{H}$. One is the weaker orbital interaction. The other is the stronger Pauli repulsion, which is caused by the larger electron density at B^0 due to the less electron-withdrawing nature of $\text{X} = \text{H}$ (see also ESI; Fig. S3†).

Finally, the case of $\text{X} = \text{F}$ is characterized by a substantially stronger orbital interaction with H_2 . This is unlike what has been observed for the attraction of noble gas atoms, which is weakest for $\text{X} = \text{F}$. This striking difference is in line with results from a recent publication,⁴³ which compared the binding of noble gases, N_2 and CO at $\text{B}_{12}\text{X}_{11}^-$. It was found that $\text{X} = \text{F}$ shows the weakest binding of noble gas atoms but the strongest binding of N_2 and CO due to π -like backbonding from B^0 into the antibonding σ^* orbitals of the attached molecule (something which is not possible for noble gases). This binding of N_2 and CO for $\text{X} = \text{F}$ is unlike the strong binding for $\text{X} = \text{CN}$, which is based almost solely on strong σ bonding, a binding mode which is much weaker for $\text{X} = \text{F}$. We expect similar behavior for the binding of H_2 , *i.e.* strong σ bonding and weak backbonding with modest H–H elongation for $\text{X} = \text{CN}$ (and to a lesser degree Cl, Br, I) and weaker σ bonding but strong backbonding for $\text{X} = \text{F}$. The stronger backbonding would also explain the much greater elongation of the H–H bond for $\text{X} = \text{F}$.

Very similar zero-point energies of attachment

Previous studies of undercoordinated metal sites show a substantial (albeit sublinear) increase of the adsorption zero-point energy with the adsorption energy in paddlewheel MOFs¹⁶ and zeolites¹⁷ (see also Fig. 2c). By contrast, all $\text{B}_{12}\text{X}_{11}^-$ investigated here have very similar zero-point energies of attachment, which are almost independent of X (see Fig. 2c).

In the case of $\text{X} \neq \text{H}$, this could be interpreted as entering a region of saturation where an increase in the attachment energy yields smaller and smaller gains in the selectivity. However, this does not explain the case of $\text{X} = \text{H}$, where a lower zero-point energy of attachment would have been expected.

An explanation is given by the ZPE contributions of the different vibrational modes (see below for a detailed discussion). The greatest ZPE variability is afforded by the asymmetrical B^0 – H stretch mode, which works in favor of the overall selectivity. However, most of this contribution is compensated by the weakening of the H–H bond with an opposite contribution (see Fig. 3b).

Vibrational modes in detail

When discussing the vibrational modes of $\text{B}_{12}\text{X}_{11}^-$, the internal rotation (φ in previous publications^{12,17}) of H_2 about the B^0 – H_2 axis is of some interest. The combination of five-fold symmetry of $\text{B}_{12}\text{X}_{11}^-$ and two-fold symmetry of H_2 results in a ten-fold internal rotational symmetry (36° period) about the B^0 – H_2 axis³¹ for homoisotopic H_2 (five-fold internal rotational symmetry for heteroisotopic H_2). The high symmetry leads to an exceptionally flat potential energy surface for this mode, which is confirmed by a scan of the potential energy surface using DFT: the obtained differences between highest and lowest energy are below 0.02 kJ mol^{-1} in all cases, which is indistinguishable from numerical noise (see NEB paths for the internal rotation in the ESI†). A comparison of the vibrational behavior of $\text{B}_{12}\text{X}_{11}(\text{H}_2)^-$ for $\varphi = 0^\circ$ and $\varphi = 90^\circ$ (equivalent to $\varphi = 18^\circ$) shows almost identical results for the frequencies of the other modes (differences of less than 5 cm^{-1}). These small differences suggest that the coupling between the quasi-free rotational mode along φ and the remaining vibrational modes is negligible. This allows for treatment of the other modes independent



of φ and thereby greatly simplifies the calculation of the ZPE and of the thermal contributions to the Gibbs energies.

H_2 coordinated at $B_{12}X_{11}^-$ exhibits a vibrational behavior that qualitatively matches that observed in previous studies of highly attractive metal centers.^{12,16} The highest-frequency mode is the H–H stretch vibration (ν_{HH} along r), which is strongly red-shifted with respect to the free molecule. It is followed by the asymmetrical B^0 –H stretch vibration ($\nu_{BH,asym}$, which in the case of weaker interaction would have been denoted as rotation of H_2 in the B^0 – H_2 plane along the angle ϑ) and the (symmetrical) stretch vibration of the B^0 – H_2 bond ($\nu_{BH,sym}$ along R).

As shown in Fig. 2b, the frequency shift of the H–H stretch vibration correlates almost linearly with the H–H distance, not only for different $B_{12}X_{11}^-$, but also when expanding the dataset using data from different $(C_4H_8O_2)M^+$ calculated in ref. 17. Near-linearity holds true even across different classes of compounds and breaks down only at extreme elongations (H_2 at $B_{12}F_{11}^-$ and $C_4H_8O_2Au^+$; the latter is not shown in Fig. 2b because of the extreme values of $\Delta r = 100$ pm and $\Delta\nu = 3722\text{ cm}^{-1}$). These cases, where the H–H stretch frequency

approaches zero and the H–H distance goes to infinity, however, are still very well described by Badger's rule,⁴⁴ which implies $\nu \propto r^{-3/2}$ for H_2 .

Likewise, it could be expected that the frequencies of the B^0 –H stretching modes correlate with the B^0 – H_2 distance. This is indeed the case for $\nu_{BH,asym}$, but surprisingly not for $\nu_{BH,sym}$.

The two remaining degrees of freedom, which can be interpreted as the hindered translations of H_2 perpendicular to the B^0 – H_2 axis, are expected to correlate more with the degree of steric hindrance than with the attractiveness of the undercoordinated site itself. Unfortunately, the substituents X are too far away from the H_2 binding site to exert any significant influence leading to little variation in the frequencies of these modes.

Zero-point energies of attachment, entropies and high predicted D_2/H_2 selectivities

Although H_2 attachment energies at $B_{12}X_{11}^-$ vary widely with X, the differences between the Gibbs energies of attachment of H_2

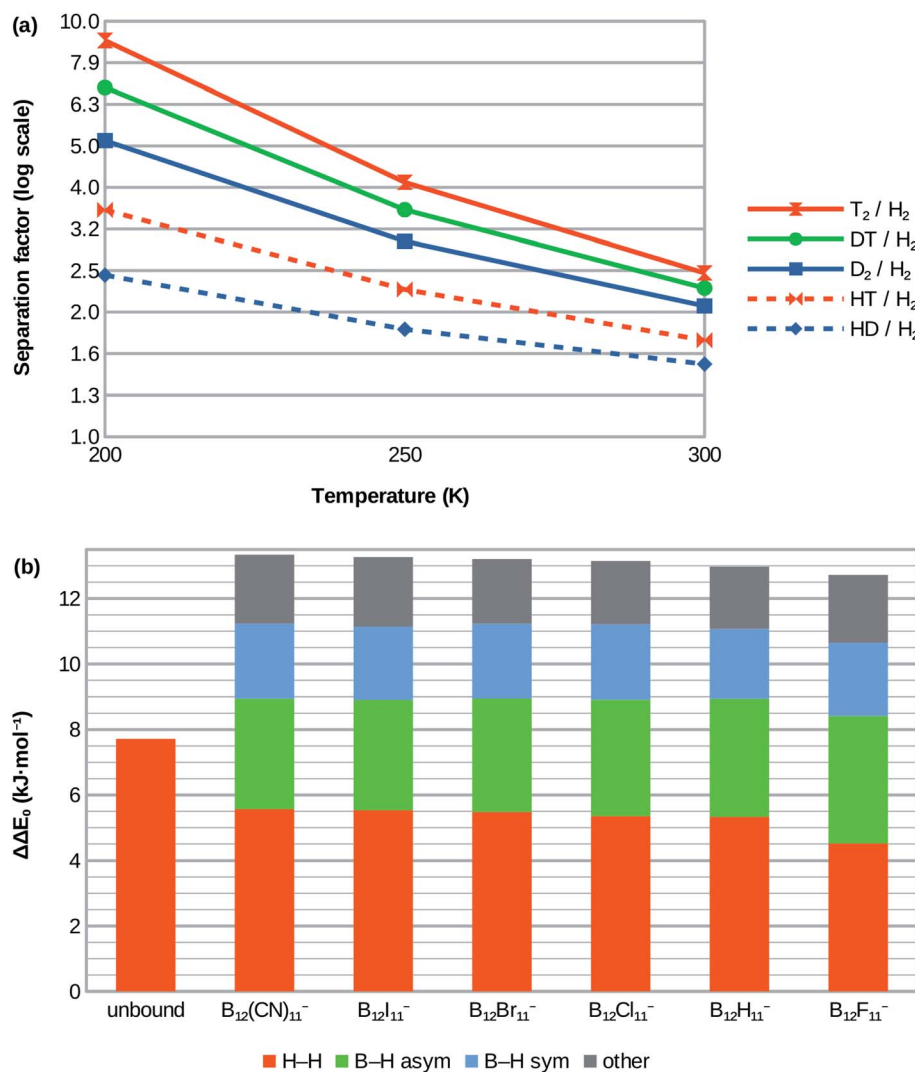


Fig. 3 (a) Calculated isotopologue selectivities for the H_2 attachment at $B_{12}X_{11}^-$ using X = Cl as example. Very similar selectivities are obtained for X = H, Br, I, CN and lower ones for X = F (see ESI; Table S1†). (b) Contribution of vibrational modes to zero-point energy difference between D_2 and H_2 isotopologues for free (unbound) dihydrogen in the gas phase (left bar) and when coordinated at the various $B_{12}X_{11}^-$.



and D_2 for a given X and therefore the selectivities are in a very narrow range (with X = F being a slight outlier). This may be surprising at the face of it, but is in line with the very similar zero-point energies of attachment of all species.

The entropy of H_2 attachment is negative because the translational and rotational entropies of the free H_2 are higher than the vibrational entropy of the bound H_2 , an effect which is more pronounced the higher the temperature. This fight against entropy is one of the key obstacles towards adsorptive H_2 isotopologue sieving at high temperatures. Therefore, the high predicted D_2/H_2 selectivity – which is approximately 2.0 at 300 K for X = H, Cl, Br, I, CN – is truly remarkable. Selectivities of about 2.9 and 5.1 are predicted for 250 K and 200 K, respectively. Note, that the selectivities at 250 K and 200 K are much higher than would be expected based on the room temperature value if only the direct influence of temperature T on the separation factor $\alpha = \exp(-\Delta\Delta G/RT)$ was considered. This is because most of the selectivity loss at higher temperatures is due to the above-mentioned entropy effects, which result in lower absolute values of $\Delta\Delta G$ as temperature increases and therefore lower selectivities.

HD/H_2 selectivities are predicted to be about 1.4 at 300 K, 1.8 at 250 K and 2.4 at 200 K. Even at 200 K, T_2/D_2 and DT/D_2 selectivities are much lower at around 1.7 and 1.3, respectively. More information is given in Fig. 3a and in the ESI (Table S1†).

Heterolytic dissociation of H_2 at $B_{12}X_{11}(H_2)^-$

Given the high H_2 binding energies, one might expect that the title compounds show a substantial propensity towards dissociation of coordinated H_2 . Indeed, we found local minimum structures with a negatively polarized H^- at B^0 and a positively polarized H^+ . As shown in Fig. 4, that H^+ can coordinate at one X (for X = F, CN), between two X (for X = Cl, Br, I) or directly at the boron core (preferred only for X = H, F), behavior which is in

line with observations on $B_{12}X_{12}H^-$ (X = F, Cl, Br, I)⁴⁵ and $B_{12}X_{11}RH^-$ (R = alkyl group).⁴⁶

The dissociation behavior of H_2 at $B_{12}X_{11}^-$ is, however, unlike what has been observed in the case of undercoordinated metal sites. In a previous publication we have predicted particularly strong H_2 interaction at zeolitic Au^+ sites¹⁷ and observed strong elongation of the H–H bond to the point of dissociation using local coupled-cluster calculations. However, dissociation was homolytic in that case and attempts to create structures with H^+/H^- polarization failed (geometry optimization reverted to structures with equivalent H atoms). This shows the uniquely strong ability of $B_{12}X_{11}^-$ to polarize H_2 and stabilize a H^- ion at the B^0 site.

For H_2 bound at $B_{12}X_{11}^-$, the activation energy for heterolytic dissociation is below (or only slightly above in the case of X = H) the H_2 attachment energy, which means that an incoming H_2 would have enough energy to overcome the barrier and dissociate. We therefore expect that $B_{12}X_{11}(H_2)^-$ (X = F, Cl, Br, I, CN) will not be observed in experiment and a technological application requiring multiple adsorption cycles is not realistic. As indicated by its potential energy surface, $B_{12}H_{11}(H_2)^-$ may be somewhat metastable against dissociation and it could therefore be interesting to study the dynamic behavior of this ion at low temperatures. Harmonic values of characteristic vibrational frequencies are given in the ESI (Table S2†).

Compared to other X, the potential energy surface for X = F is much flatter towards H_2 dissociation and the formation of the structure shown in Fig. 4(b), which is in line with the much longer H–H bond length in this case.

It is interesting to note that the heterolytic dissociation of heteronuclear H_2 isotopologues (*i.e.* HD, HT and DT) shows a preference for the heavier nucleus to occupy the position where the vibrational frequency of the corresponding stretch frequency is higher, thereby minimizing the overall zero-point energy. Especially for $B_{12}X_{11}HD^-$ with X = Cl, Br and I, this results in a pronounced preference for D to occupy the H^- position

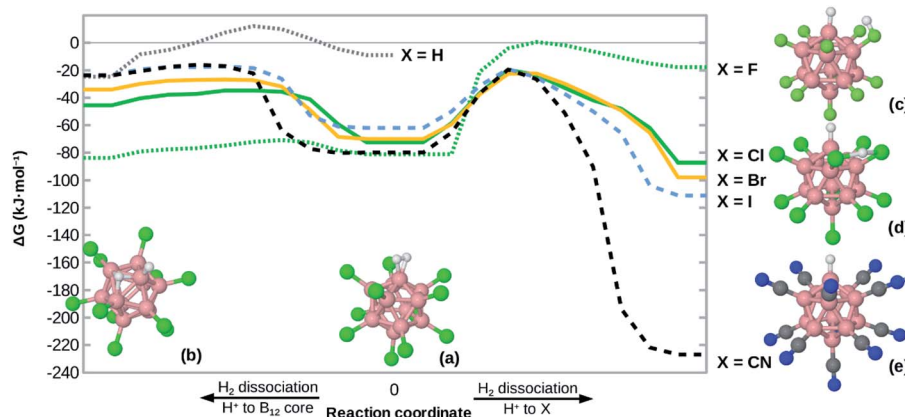


Fig. 4 Potential energy surface of H_2 bound at $B_{12}X_{11}^-$. The (local) minima in the middle (a) correspond to undissociated H_2 , the other ones (b–e) to heterolytically dissociated H_2 (with H^- at B^0). The minima on the left (b) have H^+ bound at the B_{12} cage. For the minima on the right, H^+ either binds to one X – which is a local minimum for X = F (c) and X = CN (e) – or between two X, which is a local minimum for X = Cl, Br, I (d). The curve for X = H does not show the right side as structures (a) and (c) would be equivalent in that case. Except for X = F, the two transition states shown are similar not only in energy but also in structure. The zero level of the energy corresponds to the unbound state (infinite distance between H_2 and $B_{12}X_{11}^-$). Energies for local minima are given at the DLPNO-CCSD(T)/PBE0-D3(BJ) level, other points are interpolated using PBE0-D3(BJ) data. Colors: B pinkish, H white, X green, C gray, N blue.



(coordinated at B^0 as D^-) and for H to take the H^+ position between two X as the latter is characterized by a very shallow potential energy surface. Equilibrium constants are given in Table S3.†

Related species

Preliminary calculations on related species ($B_{12}X_{11}^{2-}$, $B_{12}X_{10}^{2-}$ and $B_{12}X_{10}^-$) showed a similar propensity towards dissociative binding of H_2 , albeit with even lower dissociation barriers. Given the added computational expense of treating radical systems and/or multiple isomers, they have not been studied in detail.

For the octahedral $B_6X_5^-$, no local minimum structure with undissociated H_2 has been found at all. Their smaller structures lead to smaller B–B–B angles, stronger pre-hybridization and therefore much stronger interaction.

Conclusion

We have investigated the interaction of $B_{12}X_{11}^-$ with H_2 with a special focus on the different interaction strengths of H_2 and D_2 . Internal energies of attachment are highest for $X = CN$ and $X = F$ ($\Delta U(^1H_2) = -110 \text{ kJ mol}^{-1}$ at 0 K), decrease with increasing mass for the halogens (down to -90 kJ mol^{-1} for $X = I$) and are lowest for $X = H$ (-36 kJ mol^{-1}). Despite widely varying attachment energies, zero-point energy differences between D_2 and H_2 attachment are very similar at $\approx 5.0 \text{ kJ mol}^{-1}$ (in contrast to results from other materials where a positive correlation between both parameters was typically found). Gibbs energies for different isotopologues are reported as well, corresponding to D_2/H_2 selectivities of ≈ 2.0 at 300 K.

Unfortunately, the strong H_2 activation leads to heterolytic dissociation with activation energies below the interaction energy; that is, H_2 approaching the cluster has enough kinetic energy to overcome the activation barrier and form a compound with dissociated H_2 . This highlights the very high electrophilicity of $B_{12}X_{11}^-$ despite its negative charge, even exceeding that known from many strong H_2 -adsorbing metals like Au^+ in zeolitic environments.

Although heterolytic dissociation likely precludes experimental investigation of $B_{12}X_{11}(H_2)^-$ (with undissociated H_2) and practical application for hydrogen isotopologue separation, the example is instructive as it shows the limits of increased adsorption energy with regards to enhancing isotopologue selectivity: not only do higher adsorption energies run the risk of leading to H_2 dissociation, but there also seems to be a limit to the adsorption zero-point energy between H_2 and D_2 of around 5 kJ mol^{-1} . However, already this 5 kJ mol^{-1} difference is very encouraging as it leads to predicted D_2/H_2 separation factors of 2.0 at 300 K and 3.0 at 250 K, figures that might be further enhanced by steric confinement and would even be high enough to enable HD/H_2 separation if a suitable material could be found that does not lead to H_2 dissociation.

Outlook

Since the smaller $B_6X_5^-$ show much stronger H_2 affinity than $B_{12}X_{11}^-$, we would expect higher *closo*-borates to bind H_2 less strongly. Therefore, it could be interesting to investigate clusters like $B_{16}X_{15}^-$, $B_{32}X_{31}^-$ and $B_{42}X_{41}^-$ (which derive from

polyhedra dual to C_{28} , C_{60} and C_{70} , respectively).^{47,48} Unfortunately, the synthesis of higher *closo*-borates is faced with huge thermodynamic and kinetic obstacles.⁴⁹ To the best of our knowledge, none of these compounds have been synthesized to date, leaving little prospect for eventual application.

Nevertheless, we believe that the two known cases of $Cu(1)$ -MFU-4l (adsorption enthalpy of $\approx 35 \text{ kJ mol}^{-1}$ and appreciable selectivity around 200 K) and $B_{12}X_{11}(H_2)^-$ (internal energy adsorption of $\approx 110 \text{ kJ mol}^{-1}$ and appreciable selectivity at 300 K for $X = CN$, but dissociation and saturation of zero-point energy of adsorption) give us an estimate of the window of adsorption energies within which the search for materials enabling isotopologue-selective adsorption should be focused.

Author contributions

JW proposed to investigate the H_2 affinity of $B_{12}(CN)_{11}^-$. TW performed all calculations and prepared the first draft of the manuscript. The authors jointly discussed results and revised the manuscript.

Conflicts of interest

There are no conflicts to declare.

Acknowledgements

TW thanks the European Social Fund for a PhD fellowship. JW is grateful to a Freigeist Fellowship of the Volkswagen foundation. We thank the Center for Information Services and High Performance Computing (ZIH) at TU Dresden for computational resources.

References

- 1 M. I. Blake, H. L. Crespi and J. J. Katz, Studies with deuterated drugs, *J. Pharm. Sci.*, 1975, **64**, 367–391.
- 2 J. Atzrodt, V. Derdau, W. J. Kerr and M. Reid, Deuterium- and Tritium-Labelled Compounds: Applications in the Life Sciences, *Angew. Chem., Int. Ed.*, 2018, **57**, 1758–1784.
- 3 T. Pirali, M. Serafini, S. Cargnini and A. A. Genazzani, Applications of Deuterium in Medicinal Chemistry, *J. Med. Chem.*, 2019, **62**, 5276–5297.
- 4 J. F. Liu, S. L. Harbeson, C. L. Brummel, R. Tung, R. Silverman and D. Doller, in *Platform Technologies in Drug Discovery and Validation*, Elsevier, 2017, pp. 519–542.
- 5 A. I. Miller, *Heavy Water: A Manufacturers' Guide for the Hydrogen Century*, Published in the Canadian Nuclear Society Bulletin, 2001, vol. 22.
- 6 M. Lozada-Hidalgo, S. Hu, O. Marshall, A. Mishchenko, A. N. Grigorenko, R. A. W. Dryfe, B. Radha, I. V. Grigorieva and A. K. Geim, Sieving hydrogen isotopes through two-dimensional crystals, *Science*, 2016, **351**, 68–70.
- 7 Y. An, A. F. Oliveira, T. Brumme, A. Kuc and T. Heine, Stone-Wales Defects Cause High Proton Permeability and Isotope Selectivity of Single-Layer Graphene, *Adv. Mater.*, 2020, **32**, e2002442.



8 S. Hu, K. Gopinadhan, A. Rakowski, M. Neek-Amal, T. Heine, I. V. Grigorieva, S. J. Haigh, F. M. Peeters, A. K. Geim and M. Lozada-Hidalgo, Transport of hydrogen isotopes through interlayer spacing in van der Waals crystals, *Nat. Nanotechnol.*, 2018, **13**, 468–472.

9 J. Teufel, H. Oh, M. Hirscher, M. Wahiduzzaman, L. Zhechkov, A. Kuc, T. Heine, D. Denysenko and D. Volkmer, MFU-4 – A Metal-Organic Framework for Highly Effective H₂/D₂ Separation, *Adv. Mater.*, 2013, **25**, 635–639.

10 I. Savchenko, A. Mavrandonakis, T. Heine, H. Oh, J. Teufel and M. Hirscher, Hydrogen isotope separation in metal-organic frameworks: kinetic or chemical affinity quantum-sieving?, *Microporous Mesoporous Mater.*, 2015, **216**, 133–137.

11 S. A. FitzGerald, C. J. Pierce, J. L. C. Rowsell, E. D. Bloch and J. A. Mason, Highly selective quantum sieving of D₂ from H₂ by a metal-organic framework as determined by gas manometry and infrared spectroscopy, *J. Am. Chem. Soc.*, 2013, **135**, 9458–9464.

12 I. Weinrauch, I. Savchenko, D. Denysenko, S. M. Souliou, H.-H. Kim, M. Le Tacon, L. L. Daemen, Y. Cheng, A. Mavrandonakis, A. J. Ramirez-Cuesta, D. Volkmer, G. Schütz, M. Hirscher and T. Heine, Capture of heavy hydrogen isotopes in a metal-organic framework with active Cu(i) sites, *Nat. Commun.*, 2017, **8**, 14496.

13 H. Oh, I. Savchenko, A. Mavrandonakis, T. Heine and M. Hirscher, Highly effective hydrogen isotope separation in nanoporous metal-organic frameworks with open metal sites: direct measurement and theoretical analysis, *ACS Nano*, 2014, **8**, 761–770.

14 R. Xiong, R. Balderas Xicohténcatl, L. Zhang, P. Li, Y. Yao, G. Sang, C. Chen, T. Tang, D. Luo and M. Hirscher, Thermodynamics, kinetics and selectivity of H₂ and D₂ on zeolite 5A below 77 K, *Microporous Mesoporous Mater.*, 2018, **264**, 22–27.

15 R. Xiong, L. Zhang, P. Li, W. Luo, T. Tang, B. Ao, G. Sang, C. Chen, X. Yan, J. Chen and M. Hirscher, Highly effective hydrogen isotope separation through dihydrogen bond on Cu(i)-exchanged zeolites well above liquid nitrogen temperature, *Chem. Eng. J.*, 2020, **391**, 123485.

16 T. Wulf and T. Heine, Toward separation of hydrogen isotopologues by exploiting zero-point energy difference at strongly attractive adsorption site models, *Int. J. Quantum Chem.*, 2018, **118**, e25545.

17 T. Wulf and T. Heine, Small Crown-Ether Complexes as Molecular Models for Dihydrogen Adsorption in Undercoordinated Extraframework Cations in Zeolites, *J. Phys. Chem. C*, 2020, **124**, 9409–9415.

18 J. Warneke, G.-L. Hou, E. Aprà, C. Jenne, Z. Yang, Z. Qin, K. Kowalski, X.-B. Wang and S. S. Xantheas, Electronic Structure and Stability of B₁₂X₁₂²⁻ (X = F-At): A Combined Photoelectron Spectroscopic and Theoretical Study, *J. Am. Chem. Soc.*, 2017, **139**, 14749–14756.

19 E. Aprà, J. Warneke, S. S. Xantheas and X.-B. Wang, A benchmark photoelectron spectroscopic and theoretical study of the electronic stability of B₁₂H₁₂²⁻, *J. Chem. Phys.*, 2019, **150**, 164306.

20 V. Geis, K. Guttsche, C. Knapp, H. Scherer and R. Uzun, Synthesis and characterization of synthetically useful salts of the weakly-coordinating dianion B₁₂Cl₁₂²⁻, *Dalton Trans.*, 2009, 2687–2694.

21 M. Mayer, V. van Lessen, M. Rohdenburg, G.-L. Hou, Z. Yang, R. M. Exner, E. Aprà, V. A. Azov, S. Grabowsky, S. S. Xantheas, K. R. Asmis, X.-B. Wang, C. Jenne and J. Warneke, Rational design of an argon-binding superelectrophilic anion, *Proc. Natl. Acad. Sci. U. S. A.*, 2019, **116**, 8167–8172.

22 M. Rohdenburg, M. Mayer, M. Grellmann, C. Jenne, T. Borrman, F. Kleemiss, V. A. Azov, K. R. Asmis, S. Grabowsky and J. Warneke, Superelectrophilic Behavior of an Anion Demonstrated by the Spontaneous Binding of Noble Gases to B₁₂Cl₁₁, *Angew. Chem., Int. Ed.*, 2017, **56**, 7980–7985.

23 M. Mayer, M. Rohdenburg, V. van Lessen, M. C. Nierstenhöfer, E. Aprà, S. Grabowsky, K. R. Asmis, C. Jenne and J. Warneke, First steps towards a stable neon compound: observation and bonding analysis of B₁₂(CN)₁₁Ne, *Chem. Commun.*, 2020, **56**, 4591–4594.

24 K. Wöhner, T. Wulf, N. Vankova and T. Heine, Strong Binding of Noble Gases to B₁₂X₁₁⁻: A Theoretical Study, *J. Phys. Chem. A*, 2021, **125**, 4760–4765.

25 C. Adamo and V. Barone, Toward reliable density functional methods without adjustable parameters: The PBE0 model, *J. Chem. Phys.*, 1999, **110**, 6158–6170.

26 S. Grimme, S. Ehrlich and L. Goerigk, Effect of the damping function in dispersion corrected density functional theory, *J. Comput. Chem.*, 2011, **32**, 1456–1465.

27 F. Weigend and R. Ahlrichs, Balanced basis sets of split valence, triple zeta valence and quadruple zeta valence quality for H to Rn: Design and assessment of accuracy, *Phys. Chem. Chem. Phys.*, 2005, **7**, 3297–3305.

28 F. Neese, F. Wennmohs, A. Hansen and U. Becker, Efficient, approximate and parallel Hartree-Fock and hybrid DFT calculations. A ‘chain-of-spheres’ algorithm for the Hartree-Fock exchange, *Chem. Phys.*, 2009, **356**, 98–109.

29 F. Weigend, Accurate Coulomb-fitting basis sets for H to Rn, *Phys. Chem. Chem. Phys.*, 2006, **8**, 1057–1065.

30 S. Grimme, Supramolecular binding thermodynamics by dispersion-corrected density functional theory, *Chemistry*, 2012, **18**, 9955–9964.

31 M. K. Gilson and K. K. Irikura, Symmetry numbers for rigid, flexible, and fluxional molecules: theory and applications, *J. Phys. Chem. B*, 2010, **114**, 16304–16317.

32 C. Riplinger, B. Sandhoefer, A. Hansen and F. Neese, Natural triple excitations in local coupled cluster calculations with pair natural orbitals, *J. Chem. Phys.*, 2013, **139**, 134101.

33 Y. Guo, C. Riplinger, U. Becker, D. G. Liakos, Y. Minenkov, L. Cavallo and F. Neese, Communication: an improved linear scaling perturbative triples correction for the domain based local pair-natural orbital based singles and doubles coupled cluster method DLPNO-CCSD(T), *J. Chem. Phys.*, 2018, **148**, 11101.

34 A. Hellweg, C. Hättig, S. Höfener and W. Klopper, Optimized accurate auxiliary basis sets for RI-MP2 and RI-CC2



calculations for the atoms Rb to Rn, *Theor. Chem. Acc.*, 2007, **117**, 587–597.

35 D. G. Liakos, M. Sparta, M. K. Kesharwani, J. M. L. Martin and F. Neese, Exploring the Accuracy Limits of Local Pair Natural Orbital Coupled-Cluster Theory, *J. Chem. Theory Comput.*, 2015, **11**, 1525–1539.

36 F. Neese, Software update: the ORCA program system, version 4.0, *Wiley Interdiscip. Rev. Comput. Mol. Sci.*, 2018, **8**, 33.

37 SCM, *ADF 2019.103, Theoretical Chemistry*, Vrije Universiteit, Amsterdam, Netherlands.

38 G. te Velde, F. M. Bickelhaupt, E. J. Baerends, C. Fonseca Guerra, S. J. A. van Gisbergen, J. G. Snijders and T. Ziegler, Chemistry with ADF, *J. Comput. Chem.*, 2001, **22**, 931–967.

39 E. van Lenthe, E. J. Baerends and J. G. Snijders, Relativistic total energy using regular approximations, *J. Chem. Phys.*, 1994, **101**, 9783–9792.

40 E. van Lenthe and E. J. Baerends, Optimized Slater-type basis sets for the elements 1–118, *J. Comput. Chem.*, 2003, **24**, 1142–1156.

41 D. Denysenko, M. Grzywa, M. Tonigold, B. Streppel, I. Krkljus, M. Hirscher, E. Mugnaioli, U. Kolb, J. Hanss and D. Volkmer, Elucidating gating effects for hydrogen sorption in MFU-4-type triazolate-based metal-organic frameworks featuring different pore sizes, *Chemistry*, 2011, **17**, 1837–1848.

42 D. B. Boyd and K. B. Lipkowitz, *Reviews in computational chemistry*, Wiley-VCH, New York, 2000, vol. 15.

43 M. Mayer, M. Rohdenburg, S. Kawa, F. Horn, H. Knorke, C. Jenne, R. Tonner, K. R. Asmis and J. Warneke, Relevance of π -Backbonding for the Reactivity of Electrophilic Anions $B_{12}X_{11}^-$ ($X = F, Cl, Br, I, CN$), *Chem.-Eur. J.*, 2021, **27**, 10274–10281.

44 R. M. Badger, A Relation Between Internuclear Distances and Bond Force Constants, *J. Chem. Phys.*, 1934, **2**, 128–131.

45 C. Jenne, M. Kefler and J. Warneke, Protic anions $H(B_{12}X_{12})^-$ ($X = F, Cl, Br, I$) that act as Brønsted acids in the gas phase, *Chemistry*, 2015, **21**, 5887–5891.

46 J. Warneke, M. Mayer, M. Rohdenburg, X. Ma, J. K. Y. Liu, M. Grellmann, S. Debnath, V. A. Azov, E. Apra, R. P. Young, C. Jenne, G. E. Johnson, H. I. Kenttämaa, K. R. Asmis and J. Laskin, Direct functionalization of C–H bonds by electrophilic anions, *Proc. Natl. Acad. Sci. U. S. A.*, 2020, **117**, 23374–23379.

47 W. N. Lipscomb and L. Massa, Examples of large closo boron hydride analogs of carbon fullerenes, *Inorg. Chem.*, 1992, **31**, 2297–2299.

48 W. N. Lipscomb and L. Massa, Closo Boron Hydrides and Carbon Fullerenes, *Phosphorus, Sulfur Silicon Relat. Elem.*, 1994, **87**, 125–128.

49 P. v. R. Schleyer, K. Najafian and A. M. Mebel, The Large closo-Borane Dianions, $B(n)H(n)(2^-)$ ($n = 13–17$) Are Aromatic, Why Are They Unknown?, *Inorg. Chem.*, 1998, **37**, 6765–6772.

50 *Jmol. An open-source Java viewer for chemical structures in 3D*, <http://www.jmol.org/>.

